

EPOXI at Comet Hartley 2

Michael F. A'Hearn^{1*}, Michael J. S. Belton², W. Alan Delamere³, Lori M. Feaga¹, Donald Hampton⁴, Jochen Kissel⁵, Kenneth P. Klaasen⁶, Lucy A. McFadden^{1,7}, Karen J. Meech⁸, H. Jay Melosh^{9,10}, Peter H. Schultz¹¹, Jessica M. Sunshine¹, Peter C. Thomas¹², Joseph Veverka¹², Dennis D. Wellnitz¹, Donald K. Yeomans⁶, Sebastien Besse¹, Dennis Bodewits¹, Timothy J. Bowling¹⁰, Brian T. Carcich¹², Steven M. Collins⁶, Tony L. Farnham¹, Olivier Groussin¹³, Brendan Hermalyn¹¹, Michael S. Kelley¹, Michael S. Kelley¹⁴, Jian-Yang Li¹, Don J. Lindler¹⁵, Carey M. Lisse¹⁶, Stephanie A. McLaughlin¹, Frédéric Merlin^{1,17}, Silvia Protopapa¹, James E. Richardson¹⁰, Jade L. Williams¹

¹Department of Astronomy, University of Maryland, College Park MD 20742-2421 USA, ²Belton Space Exploration Initiatives LLC, 430 S. Randolph Way, Tucson AZ 85716 USA, ³Delamere Support Services, 525 Mapleton Ave., Boulder CO 80304 ⁴University of Alaska - Fairbanks, ⁵Max-Planck-Institut: Sonnensystemforschung, ⁶Jet Propulsion Laboratory, 4800 Oak Grove Drive, Pasadena CA 91109, ⁷NASA Goddard Space Flight Center, ⁸University of Hawaii, ⁹University of Arizona, ¹⁰Purdue University, ¹¹Department of Geological Sciences, Brown University, Providence RI 02912 USA, ¹²Cornell University, Ithaca NY, USA, ¹³Laboratoire d'Astrophysique de Marseille, Université de Provence and CNRS, Marseille, France, ¹⁴Planetary Science Division, NASA Headquarters, Mail Suite 3V71, 300 E St. SW, Washington DC 20546, ¹⁵Sigma Space Corp., 4600 Forbes Blvd., Lanham MD 20706 USA, ¹⁶JHU-Applied Physics Laboratory, 11100 Johns Hopkins Rd., Laurel MD 20723 USA, ¹⁷LESIA, Observatoire de Paris, Université Paris 7, Batiment 17, 5 place Jules Janssen, Meudon Principal Cedex 92195 France

*To whom correspondence should be addressed. E-mail: ma@astro.umd.edu

Abstract

Understanding how comets work, i.e., what drives their activity, is crucial to using comets to study the early solar system. EPOXI flew past comet 103P/Hartley 2, one with an unusually small but very active nucleus, taking both images and spectra. Unlike large, relatively inactive nuclei, this nucleus is outgassing primarily due to CO₂, which drags chunks of ice out of the nucleus. It also shows significant differences in the relative abundance of volatiles from various parts of the nucleus.

Introduction

Comets are the fundamental building blocks of the giant planets and may be an important source of water and organics on Earth. On 4 July 2005, the Deep Impact mission carried out an impact experiment on comet 9P/Tempel 1 (1,2) to study differences between the comet's surface and the interior. Although the impactor spacecraft was destroyed, the flyby spacecraft and its instruments remained healthy in its 3-year, heliocentric orbit after completion of the mission. The Deep Impact flyby spacecraft was retargeted to comet 103P/Hartley 2 as part of an extended mission named EPOXI.

The flyby spacecraft carries the High Resolution Instrument (HRI), which combines a visible-wavelength camera having pixel size $2 \mu\text{rad}$ and a set of filters with a near-IR ($1.05\text{-}4.85 \mu\text{m}$) spectrometer having an entrance slit $10 \mu\text{rad}$ by 256 mrad with 512 spatial pixels along the slit. Spectral maps are created by scanning the slit across the comet while taking a sequence of spectra. The Medium Resolution Instrument (MRI) has a pixel size $10 \mu\text{rad}$ and a different, but overlapping set of visible-wavelength filters (3,4).

Encounter with Hartley 2

Closest approach to Hartley 2 was 694 km at 13:59:47.31 UTC on 4 November 2010, one week after perihelion passage and at 1.064 AU from the sun. Flyby speed was 12.3 km/s and the spacecraft flew under the comet with a somewhat northward trajectory in a solar system reference frame. Because instruments are body-mounted on the spacecraft, the spacecraft rotated to keep the instruments pointed at the comet. Observations of the comet were carried out for 2 months on approach (5 Sep – 4 Nov) and for 3 weeks on departure (4 – 26 Nov), during which more than 10^5 images and spectra were obtained.

Prior remote sensing showed that Hartley 2's nucleus has an average radius 1/5 that of comet Tempel 1's nucleus (5,6), yet it releases more gas per unit time at perihelion, even allowing for the smaller perihelion distance of Hartley 2 (1.059 vs. 1.506 AU). This puts Hartley 2 in a different class of activity than Tempel 1 or any of the other comets visited by spacecraft (Fig. S1). The two comets have very different surface topography (Fig. 1) but whether the different topography is related to the hyperactivity is still being investigated.

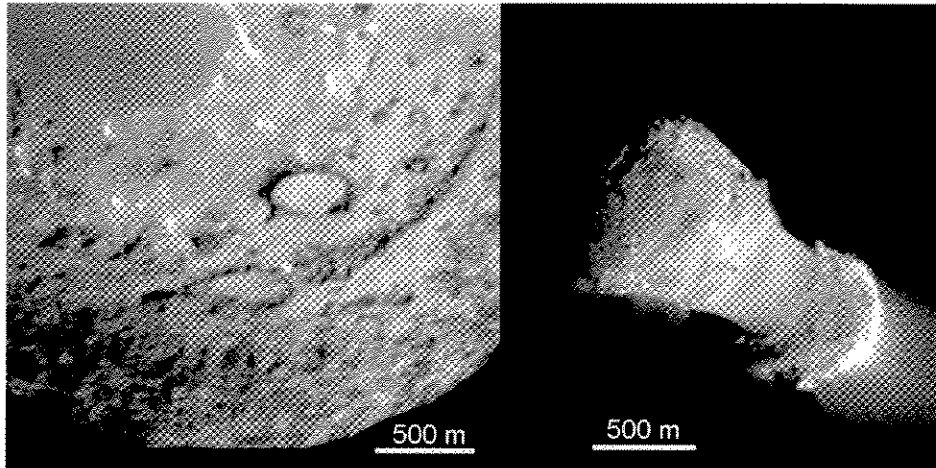


Figure 1 Comparison of a small part of Tempel 1 (left) with Hartley 2 (right) at approximately the same image scale and with nearly identical instruments. Left, Impactor Targeting Sensor (ITS) image iv9000675, 9.1 m/pixel. Right, MRI image mv5004032, 8.5 m/pixel. Sun is to the right.

The Nucleus

Spin state and variations

The rotation state of the nucleus distinguishes the morning from the evening terminator and, by comparison with longer-term coma observations, allows the number and relative strengths of active areas to be determined. Knowledge of the nuclear spin can also put constraints on internal distribution of mass in the nucleus, internal energy dissipation, and the magnitude of the net torque.

The large variations in brightness in Figure 2, reduced to a measure of the amount of dust leaving the nucleus, show a period of roughly 18 hours but the spacing of peaks in the light curve shows a clear pattern that repeats every three cycles. We interpret this (SOM) as an excited state of rotation with each cycle corresponding to precession of the long axis of the nucleus around the angular momentum vector, with a period of 18.34 hours at encounter. The pattern of 3 cycles is due to an approximate commensurability between this precession and the roll around the long axis with a period of 27.79 hours (55.42 hours is also possible; the ambiguity does not affect any conclusions in this paper). The orientation of the angular momentum vector is not yet tightly constrained but is within 10° of being perpendicular to the long axis. This excited state also implies a nodding motion of the long axis relative to the angular momentum vector but the observed near-axial symmetry of the shape limits this to an amplitude $<1^\circ$. The precession period is increasing at 0.1% per period near perihelion, an unusually high but not unprecedented rate of change for a comet. The roll period is decreasing. These changes are presumed due to torques produced by the outgassing.

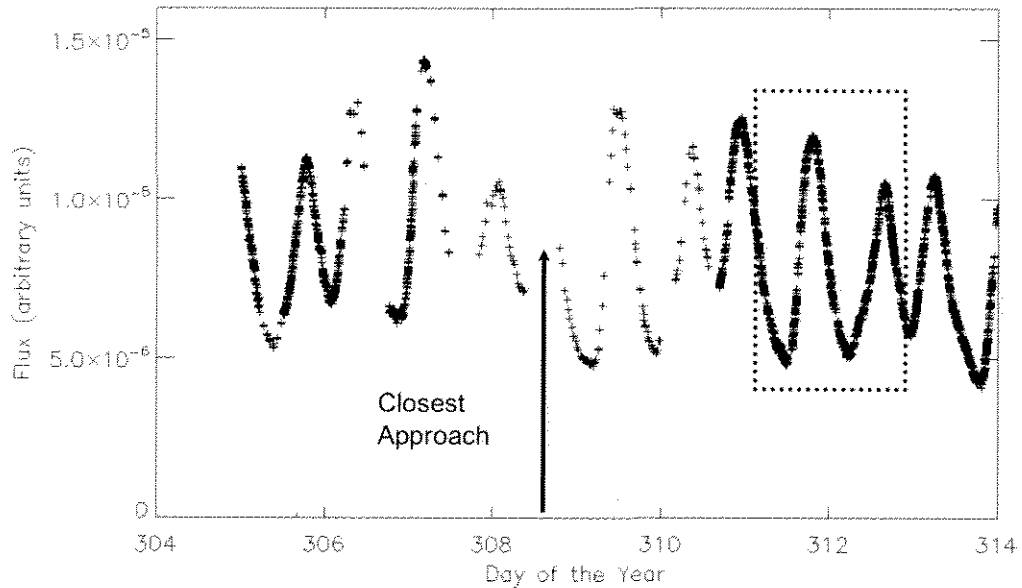


Figure 2. Variation of visible flux with time in a 191-km square aperture at the comet. Flux is proportional to the amount of dust leaving the nucleus if physical parameters of the dust do not change (no changes in dust color or other properties appear in our data nor are any reported by Earth-based observers). The dotted box is expanded later (Fig 7). Near closest approach, the flux from the nucleus is too large to allow accurate photometry of the coma.

Nuclear Shape

The nucleus is bi-lobed in shape (Fig. 1), with a maximum length of 2.33 km. The shape is well constrained by stereo viewing of nearly half the object and for much of the remainder sampled by silhouettes against the light scattered from the coma (Table 1). This bi-lobed shape is crudely similar to that of comet Borrelly (18), but is both relatively and absolutely smoother. The rotation is slow enough that gravity is sufficient to hold the two lobes together for any bulk density $>100 \text{ kg m}^{-3}$.

Table 1. Properties of Hartley 2's Nucleus			
Volume	$0.82 \pm 0.08 \text{ km}^3$	Mean Radius	$0.58 \pm 0.02 \text{ km}$
Diameter	0.69 to 2.33 km	Cross Section	$0.43\text{-}1.59 \text{ km}^2$
Surface gravity	$0.0013\text{-}0.0033 \text{ cm s}^{-2}$	Uniform density	220 kg m^{-3}
Precession Period	$18.34 \pm 0.04 \text{ h}$ (Nov 4)	Roll Period	27.79 or $55.42 \pm 0.1 \text{ hr}$
Geometric Albedo	4% (average)	Albedo range	4x

Constraints on Density

The fast (12.3 km/s) flyby did not permit determination of the nuclear mass from the spacecraft's trajectory. The smooth shape of the "waist" region connecting the two lobes might indicate material collecting in a gravitational low, such as observed on asteroid (25143) Itokawa (19). Collection could proceed by in-falling material landing in the gravitational low and/or by in situ fluidization of regolith induced by outflowing gas (20). If some form of frictionless, fluidized flow is responsible for the formation or modification of this region it should represent a 'flat' surface such that it lies along an equipotential with respect to the combined forces of both gravity and rotation. Under these assumptions, which may not be valid, the density of the nucleus can be estimated by fitting potential contours to the observed geometry of the waist (SOM).

We assumed internal homogeneity, a precession period of 18.34 hr, and a wide range of densities. The variance is minimized for a bulk density of 220 kg m^{-3} (Fig. S4). Even this minimum residual leaves large-scale slopes of up to a few degrees relative to the equipotential. A reasonable lower limit for the density is 180 kg m^{-3} because the waist is no longer a gravitational low for lower densities. The upper limit is not well determined but a 4x increase above the best fit density to 880 kg m^{-3} requires modest porosity for pure ice and significant porosity for plausible rock/ice mixtures.

Any interpretation rests on the character of the surface at the waist, which is mottled on horizontal scales of 10-30 m, and has some isolated cases of local relief > 10 m. The mottling, local topography, and generally gradational boundary distinguishes the waist from the best observed flow on Tempel 1 (1) and the ponded materials on (433) Eros (26) and on Itokawa (19) at least locally, but does not rule out the possibility that the overall shape of the waist is approximately an equipotential. If the surface in this region approaches an equipotential and was formed by flows or by deposition similar to those on other objects, it has subsequently evolved, suffering several m of erosional etching. These facts suggest that the equipotential assumption may not be reliable and that, unlike the case for Tempel 1 where a different and more direct approach was possible (21), the density might be significantly higher than deduced under our assumptions.

Geology of Surface

The nucleus has two primary terrain types (Fig. 3a): knobby terrain characterized by rounded to angular elevated forms up to 50 m high and 80 m wide and relatively smooth regions occupying both the waist (Fig. 3c) between the two lobes and parts of the larger lobe (Fig. 3b). The elevated forms appear to be the larger members of a population with most examples near or below our practical mapping resolution (~12 m; e.g. Fig. 3d). The smoother areas have darker central regions, are elongate, and are partially bounded by strings of the elevated forms that make up the knobby terrain. There is marginally resolved mottling of the smooth regions on the larger lobe, and better resolved mottling and local topography of 10-30 m scale in the waist. The darkest regions of the larger lobe are slightly more sharply bounded than is the darker band within the waist. The elevated forms that constitute the rough terrain are in some areas aligned along boundaries of albedo markings, and follow much of the southern edge of the "waist." Many of the elevated forms exhibit 2 to 3 times higher albedo than the average, a much greater range

than seen on Tempel 1. Ragged, somewhat sinuous, narrow depressions are visible at high incidence angles near the southern end, about 10 m deep, up to 90 m wide, and extending for over 250 m.



Figure 3. Hartley 2, image mv600002, ~ 7 m/pixel. Sun is to the right and the positive rotational pole is at the smaller (right) end. The view is from latitude ~ -33°.

The average geometric albedo of the nucleus is ~4%. Within the larger lobe area are several roughly equidimensional spots < 80 m across that appear even darker than the larger, more elongated “dark” areas mentioned above (Fig. 3e). The darkest unshadowed spots are less than half the average brightness. While we can not rule out steep sided holes for the dark spots near the terminator, they generally occur in regions that are smooth in stereo and show no shadow signatures. Thus local albedos span at least a factor 4, compared to <2 on Tempel 1.

Jets occur in all terrains, but are clustered in the rough topography of the smaller lobe and mid- to northern part of the larger lobe (Fig. 3, also Fig. 5). Such clustering of jets has also been seen at comet 1P/Halley (27). At least some jets appear to originate at or near large, bright elevated forms. Jets also originate beyond the terminator in areas with no direct sunlight, such as along the lower edge of the larger lobe in Fig. 4. Even our resolution of 10-12m is not sufficient to clearly resolve the morphology of the sources of the jets.

This comet lacks a population of depressions such as those that dominate 81P/Wild 2 (28), or those scattered across Tempel 1 (1,29). The knobby terrain is similar to some of

the rougher areas on Tempel 1. The smoother regions on Hartley 2 do not show the striations suggestive of flow markings on the best observed such region on Tempel 1, and they are more gradationally bounded. The combination of terrains is very different from Tempel 1 or Wild 2, and this comet lacks exposures of thick, internal layers that were prominent on Tempel 1.

Nuclear Activity

CN Anomaly

Gaseous CN abundances were measured routinely from the start of observations on 5 Sep (SOM). The long-term CN gas production gradually increased from $6 \times 10^{24} \text{ s}^{-1}$ on 5 Sep to a peak of $3 \times 10^{25} \text{ s}^{-1}$ at perihelion (28 Oct), after which it decreased again to $\sim 2.4 \times 10^{25} \text{ s}^{-1}$ at closest approach and $1.2 \times 10^{25} \text{ s}^{-1}$ on 25 Nov (Fig. S5). During most of the encounter the CN production varied periodically with the precession of the nucleus, as did the grains and other gases.

The production of CN also exhibited an anomalous increase, by a factor of ~ 7 , between 9 and 17 Sep. after which it slowly decreased, returning to the long-term trend line by 24 Sep (Fig. S5). There was a very weak increase in dust release ($\Delta A(\theta)_{fp} < 10 \text{ cm}$) above its trend in that same period. There was no corresponding increase of water (34). Integrating over the period 9-24 Sep. and subtracting a baseline gas production rate of $7 \times 10^{24} \text{ s}^{-1}$, we find that $\sim 2 \times 10^{31}$ CN radicals (~ 800 tons) were released in the anomaly.

The long-duration, gradual increase and decrease of gaseous emission without a corresponding increase in the dust production is atypical of cometary outbursts, which have sudden onsets and are usually accompanied by considerable dust. The increase is unlike the activity observed at 9P/Tempel 1 or the behavior of any other comet. The spatial profile of CN during the anomaly was very different from that during the rest of the observations and suggests formation of CN from some extended source other than photodissociation of HCN. This could be grains too dark to scatter much sunlight such as HCN polymers (35) or the CHON grains found at 1P/Halley (36). They would need to be lifted by something abundant and volatile.

Large Chunks

Radar observations in October showed an ensemble of particles $>$ a few cm (12, 37). While clouds of large particles had been reported previously from radar measurements of other comets (38), the location relative to the nucleus and the composition are not known. Previous searches with remote sensing for an icy grain halo in comets have rarely been successful with the only detections being at large heliocentric distances (39-41).

At EPOXI's close approach, individual chunks were seen near the nucleus in many images from both MRI and HRI (Fig. 4). The motion of the spacecraft allowed determination of the positions of individual chunks and their motions. A sample of 50 chunks has been followed in many different MRI images and, other than one at 28 km, all

were found to be within 15 km of the large end of the nucleus. The motions are all very slow, 80% moving at less than 0.5 m s^{-1} and the fastest moving at $<2 \text{ m s}^{-1}$. This implies minimum lifetimes of 10^4 s for many of the chunks. Escape velocity is poorly defined near the surface because of the rotating, elongated shape as well as the uncertainty in the mass of the nucleus. We estimate that 10-20% of the chunks are moving at less than their local escape velocity.

Sizes are estimated from the brightness of the chunks (SOM). The apparent flux from each of $>10^4$ individual chunks ranges from $\sim 10^{-13}$ to $<10^{-11} \text{ W m}^{-2} \mu\text{m}^{-1}$ in the HRI image in Fig. 4, similar to that measured in the MRI image taken close in time (Fig. 4). Sampling below $10^{-12} \text{ W m}^{-2} \mu\text{m}^{-1}$ is incomplete. We considered two extreme cases for the scattering properties – icy chunks scattering with the albedo and phase function of Europa (42-43) and dirty chunks scattering with the albedo and phase function of the nucleus of comet Tempel 1 (44). The range of measured fluxes corresponds to radii of 10-150 cm if they are dirty chunks and 1-15 cm if they are ice (nearly pure). Below the minimum size the chunks blend into the background of unresolved, smaller chunks or grains. Since meter-sized objects are at the extreme of what can be lifted by gas drag and since the smaller, unresolved chunks are demonstrably icy (see below) we argue that the largest chunks are icy and roughly 10-20 cm in radius.

The size distribution implied by the fluxes of the discrete chunks is unusually steep. Most of the mass and most of the cross-section are in the smallest grains. The discrete chunks contribute roughly 4% of the total surface brightness in the innermost coma ($<5 \text{ km}$) and those $>\sim 5 \text{ cm}$ (completeness limit) are widely spaced at $4 \times 10^{-8} \text{ m}^{-3}$. If we extrapolate the size distribution (SOM) we find that $>100\%$ of the surface brightness is accounted for just with chunks $>0.5 \text{ mm}$. The total cross section of discrete chunks, roughly the same size chunks as ones to which radar is sensitive, is very small compared to that detected by radar (12, 37), which presumably is detecting much darker chunks over a much larger field of view.



Figure 4. Original HRI image (left, hv5004024, E-66s, range 915 km). Deconvolved image in center. Rightmost panel is an MRI context image (mv5004029) showing the location of the HRI field above the large lobe of the nucleus. Arrows indicate projected directions to Sun and Earth.

Heterogeneity of Dominant Volatiles

Spectral scans of the comet were obtained from 1 Oct to 26 Nov, including several in which the nucleus was spatially resolved. Figure 5 is from a scan taken 7 minutes after closest approach with an MRI image taken at nearly the same time. Red boxes show regions where we have extracted the two spectra shown in Figure 6, both of which have had the continuum removed manually. The ratio of the H₂O band to the CO₂ band varies by 2.9× spatially. In these maps (Fig. 5), the emission bands of H₂O and CO₂ are both somewhat optically thick, implying that variations in column density could be larger than in brightness.

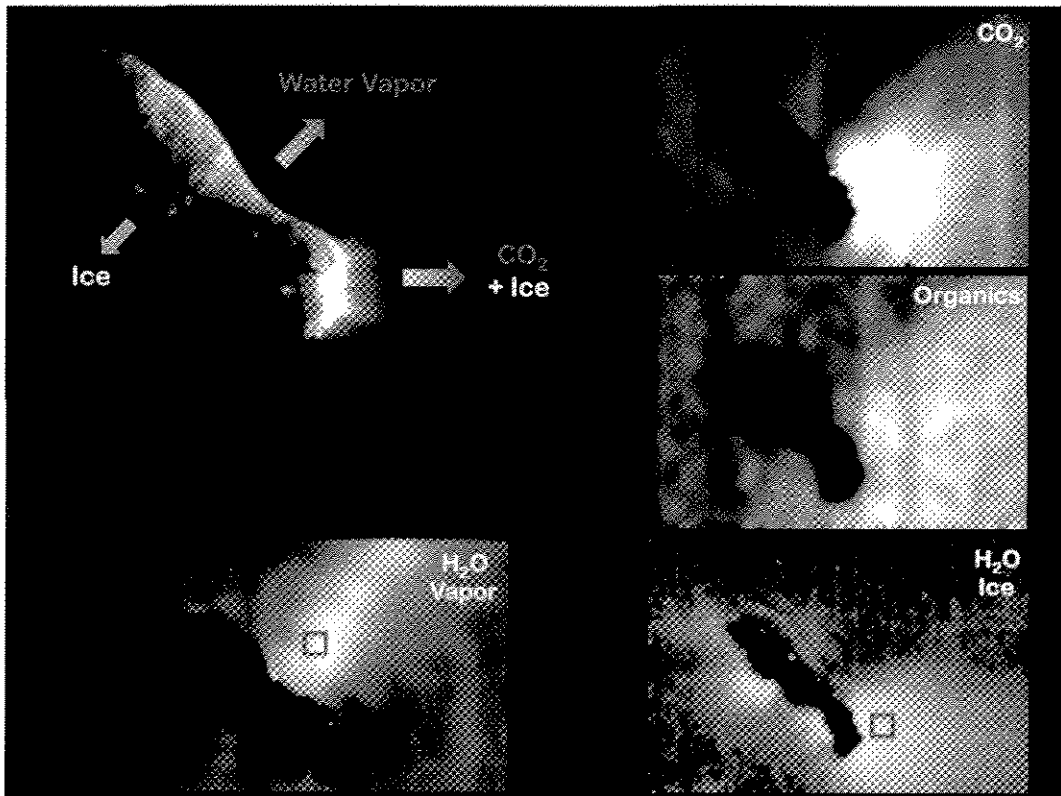


Figure 5. Relative spatial distribution in the coma of Hartley 2. The red boxes (5x5 pixels; 52 m/pixel) indicate regions sampled to produce the spectra in Figure 6. Panels labeled CO₂, Organics, and H₂O Vapor are maps of the total flux in the relevant emission bands. The panel labeled H₂O Ice is a map of the depth of the ice absorption feature at 3 μm. Each panel has been individually linearly stretched. All spectral images are from a scan at E+7 min, hi5006000. Sun is to the right.

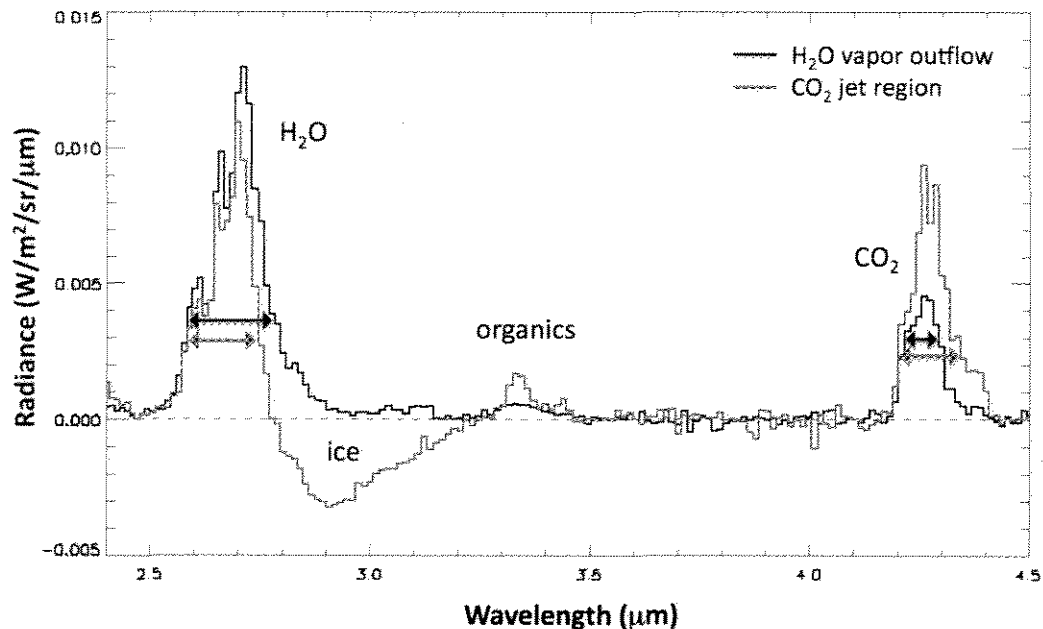


Figure 6. Absolute spectra in the coma of Hartley 2 at CA+7 min. The black curve is the water-rich but ice-free spectrum from the box in the panel “H₂O Vapor” in Figure 5, above the waist of the nucleus. The red curve is the ice-rich spectrum from the box in the panel “H₂O Ice” in Figure 5, the jet region near the small end of the nucleus.

The maps show a water-vapor-rich region extending roughly perpendicular to the waist of the nucleus and presumably arising from the waist. This region has relatively little CO₂, relatively little gaseous organics, and thus far no detectable water ice. The region of the jets off the end of the smaller lobe of the nucleus is rich in CO₂, rich in organics, and rich in water ice but with a lower column density of water vapor than above the waist. There is significant ice in jets emanating from beyond the terminator along the lower edge of the larger lobe of the nucleus. The boundaries and the direct association with the major units of the nucleus seen here are dramatic and suggest very different histories for the waist and the remainder of the nucleus. The coincidence of strong absorption bands of ice with jets that are bright in the continuum suggests that jets are bright when highly reflective ice is present in the jets, and conversely that jets are usually fainter than the nucleus because they are of optically thin, relatively dark material.

Theoretical calculations of scattering by icy grains (SOM) show that the predominant scattering grains must be smaller than 10 μm. However, >100% of the surface brightness can be accounted for by extrapolating the chunks to a size of 0.4 mm, implying that the chunks are fluffy aggregates or clusters of ~1-μm solid grains. Either most of the aggregates of order 1-mm have broken up or they mimic the scattering of the small grains. This result is very similar to the result obtained at Tempel 1 after the impact (no ice was observed prior to the impact). Those grains were predominantly micron-sized (47). The similarity between excavated material from Tempel 1 and ambient outgassing from Hartley 2 suggests that the constituent grains of solid ice are of order a micron in

most comets. Based on calculations of lifetimes (48-50) for the <10- μm solid components, the ice must be nearly pure for the grains to persist.

The detection of strong absorption by ice, the detection of very large chunks in the coma, the concentration of all species other than H_2O vapor away from the waist of the nucleus, and the relatively smooth surface of the waist lead us to suggest that the material at the waist has been redeposited as a mixture of dirty grains and fluffy, icy aggregates that have not yet sublimed. The warmth of the dirty grains then leads to sublimation of the icy grains just below the surface. We conclude that this aspect of the chemical heterogeneity of the nucleus of Hartley 2 is likely evolutionary.

To determine the absolute abundance ratio, we considered a spectral map made three rotations (55 hours) earlier, when both the precession and roll orientations were the same. Spectra were extracted from a 120-km box and from a 600-km box, both centered on the brightest pixel of thermal emission (a better proxy for the nucleus than a reflected light center). In an aperture of 600×600 km centered on the nucleus (Fig. S8), and assuming an outflow speed of 0.5 km/s we find average production rates, $Q(\text{H}_2\text{O}) = 1.0 \times 10^{28} \text{ s}^{-1}$ and $Q(\text{CO}_2) = 2.0 \times 10^{27} \text{ s}^{-1}$ for ~20% fraction of CO_2 . This is higher than the fraction obtained in previous measurements of the global production of CO_2 in this comet (51-53).

In Figure 7 we compare a portion of the visual light curve with the variation of CO_2 and H_2O from the spectral scans. The scale is arbitrary so only relative variations are meaningful. The ratio $\text{CO}_2/\text{H}_2\text{O}$ varies by a factor 2 between maxima and minima. The lower portion of Figure 7 shows images of the CO_2 and the H_2O from the spectral maps. The red line indicates the position of the nucleus as defined by the peak thermal pixel. Close inspection shows that CO_2 is more sunward (up in the figure) than H_2O near the maxima, reflecting the different spatial distributions. This suggests that the $\text{CO}_2/\text{H}_2\text{O}$ ratio is less in the large lobe of the nucleus than the small lobe, but this is a very tentative conclusion until the rotational state is fully understood. If true, this heterogeneity is almost certainly primordial, unlike the ambiguous interpretation for the heterogeneity of Tempel 1 (52).

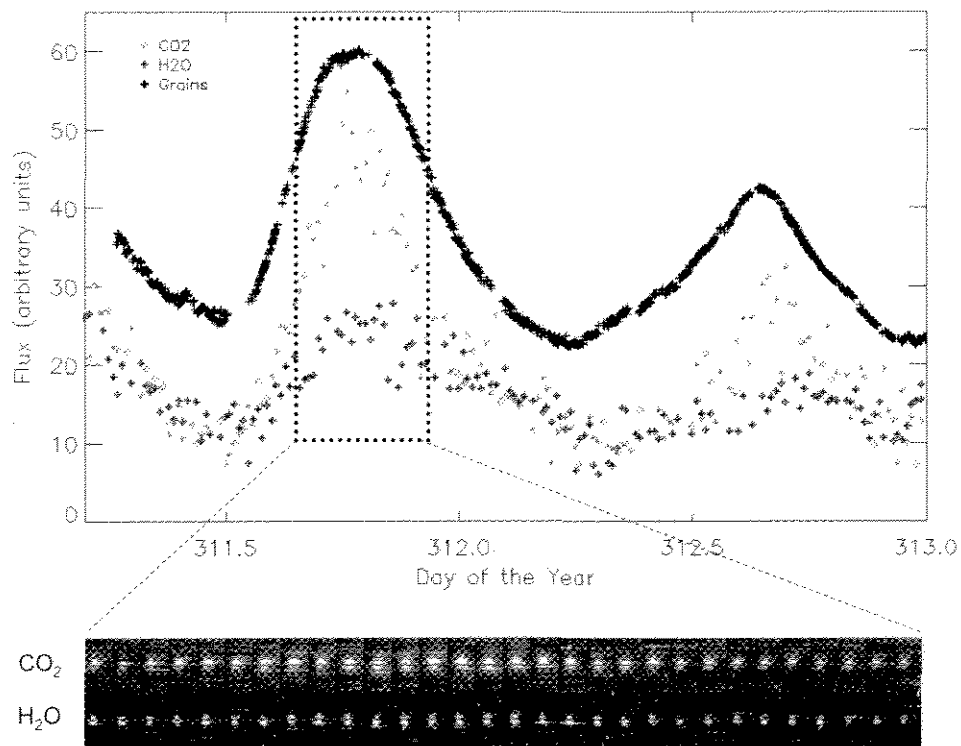


Figure 7. Light curve in visible light compared with light curve in H₂O and CO₂. The curve for grains is an expanded version of the box in Figure 2. The data-points for gas are derived from spectral maps. The lower portion shows an expanded view with images of the CO₂ and H₂O for each point in the dotted box. The centroid of reflected continuum in each scan has been aligned with the red, horizontal line. The sun is up in the small images of gas.

Summary & Conclusions

Comet 103P/Hartley 2 differs in many ways from 9P/Tempel 1 and is an ideal example of hyperactive comets, ones that produce more H₂O per unit time than should be possible by sublimation from the small surface area of their nuclei. Super-volatiles, specifically CO₂ in the case of Hartley 2, are the primary drivers of activity. The super-volatiles drag out chunks of nearly pure water-ice, which then sublime to provide a large fraction of the total H₂O gaseous output of the comet. Other hyperactive comets include 46P/Wirtanen and 21P/Giacobini-Zinner.

In Hartley 2, H₂O sublimates from the waist with much lower content of CO₂ and barely any trace of icy grains. We tentatively interpret the waist as a secondary deposit of material, although the mechanism of redeposition remains unclear. The most likely mechanism involves fallback of both refractories and icy chunks from the periphery of the active regions. CO₂/H₂O varies by a factor 2, likely between one end and the other.

From HST measurements (55), CO < 0.3%, implying CO₂/CO > 60, a far more oxidized environment than is consistent with any model of the outer protoplanetary disk.

This is also different from Tempel 1 (~1) (54) and Halley (<1) (56). A large anomaly in CN, too slow to be called an outburst, is unexplained.

References and Notes

- [1] M. F. A'Hearn et al., *Science* **310**, 258 (2005).
- [2] M. F. A'Hearn & M. R. Combi (Eds.) *Icarus* **191** (2007).
- [3] D. L. Hampton et al. *SpaceSci.Rev.* **117**, 43 (2005).
- [4] K. P. Klaasen et al. *Rev.Sci.Instr.* **79**, 091301 (2008).
- [5] O. Groussin et al., *Astron.Astrophys.* **419**, 375 (2004).
- [6] C. M. Lisse et al. *Pub.Astron.Soc.Pac.* **121**, 968 (2009).
- [7] M. J. S. Belton, In *Comets in the Post-Halley Era* Ed. R. L. Newburn et al. (Kluwer: Dordrecht) v2, p697 (1991).
- [8] N. H. Samarasinha, M. F. A'Hearn *Icarus* **93**, 194 (1991).
- [9] N. H. Samarasinha et al., In *Comets II*, Ed. M. C. Festou et al. (Univ. Arizona Press: Tucson) p281 (2005).
- [10] M. J. S. Belton et al. *Icarus* DOI: 10.1016/j.icarus.2011.01.006 (2011)
- [11] K.J. Meech et al., *IAU Circ. #9163* (2010).
- [12] J.K. Harmon et al., *IAU Circ. #9179* (2010).
- [13] N.H. Samarasinha et al., *IAU Circ #9178* (2010).
- [14] E. Jehin et al., *CBET #2589* (2010).
- [15] M. Knight, D. Schleicher, *IAU Circ. #9163* (2010).
- [16] M.J.S. Belton et al., *Icarus*, **95**, 183 (1991).
- [17] N.H. Samarasinha, M.J.S. Belton. *Icarus* **116**, 340 (1995)
- [18] L. Soderblom et al., *Science* **296**, 1087 (2002).
- [19] A. Fujiwara et al., *Science* **312**, 1330 (2006).
- [20] M. J. S. Belton, J. Melosh *Icarus* **200**, 280 (2009).
- [21] J. E. Richardson et al. *Icarus* **190**, 357.
- [22] B. J. R. Davidsson et al. *Icarus* **187**, 306 (2007).
- [23] B. J. R. Davidsson, P. J. Gutiérrez. *Icarus* **180**, 224 (2006).
- [24] B. J. R. Davidsson, P. J. Gutiérrez. *Icarus* **168**, 392 (2004).
- [25] T. L. Farnham, A. L. Cochran. *Icarus* **160**, 398 (2002).
- [26] M. S. Robinson et al., *Nature* **413**, 396 (2001).
- [27] H. U. Keller et al. *Astron.Astrophys.* **187**, 107 (1987).
- [28] D. E. Brownlee, et al.. *Science* **304**, 1764-1769 (2004).
- [29] P. C. Thomas et al. *Icarus* **187**, 4 (2007).
- [30] D. G. Schleicher , *Astron. J.* **140**, 973 (2010).
- [31] L. Haser, *Bull.Cl.Sci.Acad.R.Liege* **43**, 740 (1957).
- [32] M. C. Festou *Astron.Astrophys.* **95**, 69 (1984).
- [33] M. F. A'Hearn et al., *Astron.J.* **89**, 579 (1984).
- [34] M. R. Combi et al., *Astrophys.J.Lett* in press (2011).
- [35] C. N. Matthews, R. Ludicky *Adv. Space Res.* **12**, 21 (1992)
- [36] J. Kissel et al. *Nature* **321**, 336 (1986).
- [37] J. K. Harmon et al. *Astrophys.J.Lett* in press (2011).
- [38] J. K. Harmon et al. In *Comets II* Ed. M. C. Festou et al. (Univ. Arizona Press: Tucson) p274 (2005).

- [39] M. F. A'Hearn et al. *Astrophys. J. Lett.* **248**, L147 (1981)
- [40] H. Campins et al. *Nature* **301**, 405 (1983).
- [41] M. S. Hanner *Astrophys. J. Lett.* **277**, L78 (1984).
- [42] W. M. Grundy et al. *Science* **318**, 234 (2007)
- [43] B. Buratti, J. Veverka *Icarus* **55**, 93 (1984)
- [44] J.-Y. Li et al. *Icarus* **187**, 141 (2007)
- [45] S. G. Warren, R.E. Brandt *J.Geophys.Res.* **113**, D14220 (2008).
- [46] B. Hapke *Theory of Reflectance and Emittance Spectroscopy* (Cambridge Univ. Press: Cambridge UK) (1993).
- [47] J. M. Sunshine et al. *Icarus* **190**, 284 (2007)
- [48] H. Patashnick, G. Rupprecht *Icarus* **30**, 402 (1977)
- [49] M. S. Hanner *Icarus* **47**, 342 (1981)
- [50] H. I. M. Lichtenegger, N. I. Kömle *Icarus* **90**, 319 (1991)
- [51] H. A. Weaver et al. *Astrophys. J.* **422**, 374 (1994)
- [52] L. Colangeli et al. *Astron. Astrophys.* **343**, L87 (1999).
- [53] J. Crovisier et al. In *ESA SP 427*, 161 (1999).
- [54] L. M. Feaga et al. *Icarus* **190**, 345 (2007).
- [55] H. A. Weaver et al. *Astrophys.J.Lett* in press (2011).
- [56] D. Bockelée-Morvan et al. In *Comets II* Ed. M. C. Festou et al. (Univ. Arizona Press: Tucson) p391 (2005).

Data from EPOXI will be released through NASA's Planetary Data System in 2011. Image IDs in this paper are part of the final ID in the archive. This was supported by NASA's Discovery Program contract NNM07AA99C to the University of Maryland and task order NMO711002 to the Jet Propulsion Laboratory. The work was supported by the home institutions of several of the scientists, particularly by the University of Maryland. The contributions of O. Groussin and F. Merlin to this project were funded in part by the Centre National d'Etudes Spatiales (CNES).

Supplementary On-line Material

Global Comparison

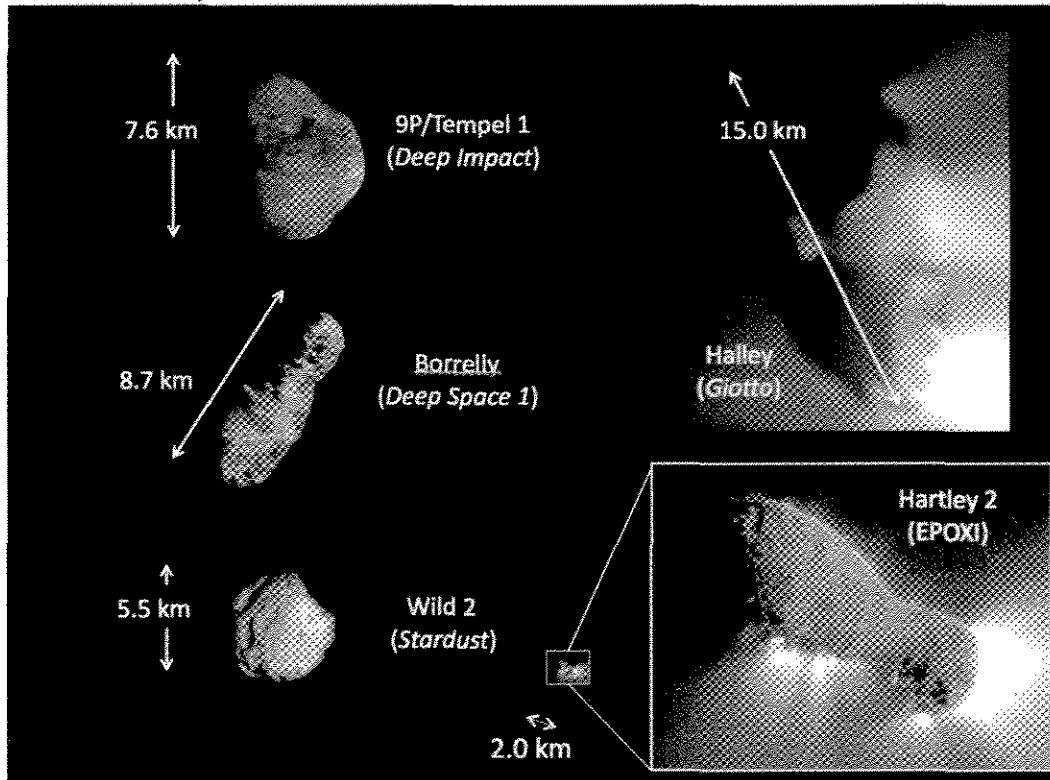


Figure S1. Images at the same scale for all cometary nuclei observed by spacecraft. Differences in overall shape are dramatic, as are the differences in contrast between the nuclei and their associated jets, which are brighter than the nucleus at Halley and Hartley 2 and much fainter than the nucleus at the other comets.

Rotational State

For background discussion of excited states of rotation in the context of small bodies, and in particular the choice of terminology, see (7-9). These references also include the background mathematical derivations. Our discussion is based on a Long Axis Mode (LAM) as described in those references since this is far more likely dynamically possible than a short-axis mode (SAM) based on the observed properties, including the observed axial ratios.

Periodogram analysis of the light curve on approach revealed seven periods in the earliest data, from E-60 to E-40 d (E = time of encounter), of which six are shown in Figure S2. Subsequent accumulating data then showed that these periods were changing over the course of the encounter (Fig. S2). Periods P2 and P4 increase with time and are associated with the precession period of the long axis around the angular momentum vector and its first sub-harmonic. Thus the period of precession of the long-axis is varying from <17 to >18 hours, with a value 18.34 ± 0.04 h at encounter. The observed motion of the nucleus in the short interval over which the nucleus was clearly spatially resolved is consistent with P2 but not with P4 as the true precession period. Furthermore, the morphology of the coma as seen from ground-based telescopes also repeats approximately (but not exactly) with the period P2. The variation of P2 with time is shown in more detail in Figure S3, where we have included several published values from Earth-based observatories.

Periods P1, P3, P5, and P6 decrease with time (Fig. S2, Table S1) and are associated with the roll around the long axis. We adopt $P3 = 27.79 \pm 0.31$ h at encounter as the roll period. P1 has very low power in the periodogram analysis and is therefore likely a harmonic, but P5 has power comparable to P3 and can not be excluded as the true period. Since the roll around the long axis has low linear speeds at the surface, the motion can not be seen in our resolved images. The ambiguity has no effect on any of our conclusions in this paper. The rates of change of the periods, determined from fitting a straight line to the data in Figure S2, are given in Table S1. P7 is relatively weak, approximately $8 \times P2$ and off scale in Fig. S2.

As a first approximation, the spatial orientation of the rotation state has been determined assuming that the end of the long axis traces out a great circle on the sky. This is equivalent to assuming that the rotation is not excited, a reasonable first approximation since our subsequent studies show that the excitation is small. We constrained the direction of the total angular momentum vector by the change in position angle of the projected axis of figure of the nucleus and its apparent length on approach to encounter. In a set of 11 resolved and deconvolved HRI images¹ from the last hour of approach, the actual orientation of the long axis moved over an 18° arc on the sky, which constrained the direction of the total Angular Momentum Vector (AMV) to RA, Dec = $59^\circ, 55^\circ \pm 2^\circ$ in this approximation. At encounter (JD2455505.08318) the small, active end of the long axis points towards RA, Dec = $226.1^\circ, 39.4^\circ (\pm 0.7^\circ \text{ circular error})$.

Although the roll period is still uncertain it is possible to conclude that the excitation is not extreme based on ratios of the principal moments of inertia obtained from the shape

model under the assumption of a homogeneous mass distribution in the interior. Using the theory of force-free rigid body rotation (8), we find that the long axis should be inclined to the AMV by $>80^\circ$ and that any “nodding” motion of this axis should have an amplitude $< 1^\circ$, too small to be detectable in our data. The excited spin state is still being evaluated and we expect that the excited solution will displace the orientation of the AMV by $< \sim 20^\circ$.

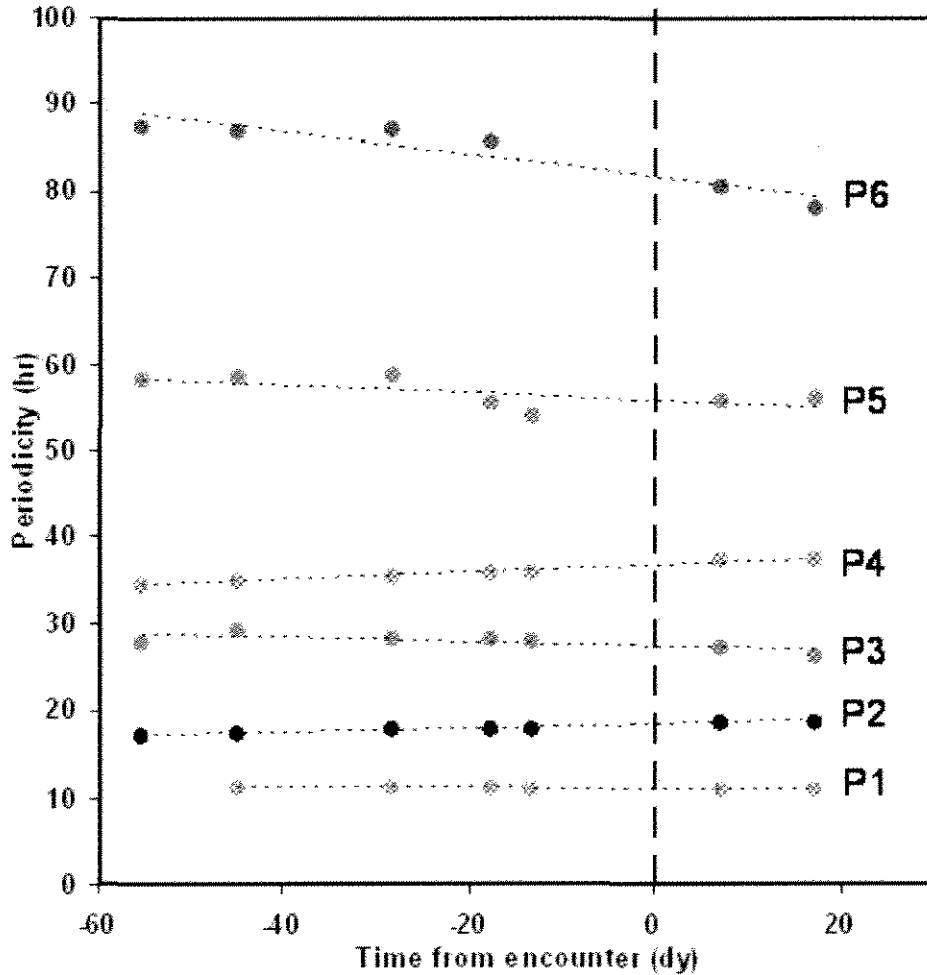


Figure S2. Variation of the periodicities seen in the light-curve of the comet through the EPOXI/DIXI encounter. The periodicities P2 and P4 increase with time (a third, longer period that increases with time, P7, is not shown here in order to increase the clarity of the presentation); the remaining periodicities, P1, P3, P5, and P6, decrease with time. We associate the former group with the precession of the long axis of the nucleus around the total angular momentum vector and the latter group with the spin component around the long axis.

Weighted Trend-Line Parameters for 103P/Hartley 2				
#	Frequency		Period	
	Slope x 10 ⁶ (hr ⁻¹ /dy)	Intercept (hr ⁻¹)	Slope x 10 ³ (hr ⁻¹ /dy)	Intercept (hr)
f ₁	+2 ± 17	0.0901 ± 0.0004	-0.5 ± 2	11.09 ± 0.05
f ₂	-72 ± 7	0.0543 ± 0.0001	+24 ± 2	18.34 ± 0.04
f ₃	+21 ± 17	0.0360 ± 0.0004	-17 ± 13	27.79 ± 0.31
f ₄	-37 ± 3	0.0272 ± 0.0001	+49 ± 4	36.73 ± 0.08
f ₅	+4 ± 2	0.0180 ± 0.0003	-5 ± 7	55.42 ± 0.10
f ₆	+22 ± 5	0.0121 ± 0.0001	-165 ± 32	82.64 ± 0.57

Table S1. Weighted slopes and S2 and S3. The intercepts represent our best estimates of the component periodicities at encounter. The form of the trend-line is $y = \text{slope} \cdot x + y_0$ where x is days from encounter and y_0 is the intercept at encounter (JD 2455505.08318). The number (#) of the periodicity is given in column 1 and shown in Figures S2 and S3.

Our estimates of the total angular momentum and total rotational energy per unit mass are $\sim 1.1 \times 10^5 \text{ m}^2 \text{ h}^{-1}$ and $\sim 2 \times 10^4 \text{ m}^2 \text{ h}^{-2}$ and these are changing at the rather substantial rates of $\sim 0.1\%/d$ and $\sim 0.2\%/d$, respectively. The change in rotational period (or angular momentum) of Tempel 1, for comparison, is $\sim 0.02\%$ per day near perihelion (10). The harmonic relationships between the periodicities are quite clear in the data with a strong first sub-harmonic of both the precession and roll periods appearing in the periodograms. The rapid change in the periods and the temporal changes in the non-gravitational acceleration of the comet in its orbit both are indicative of the combination of a high outgassing rate coupled with a small mass and, for the periods, a very elongated shape. Figure S3 combines our data on the precessional period, P2, with a variety of other observations (11-15) and shows that the precessional period remains constant while the comet is far from the sun and inactive but that it changes rapidly around perihelion while the comet is active. Finally, the precession and roll periods appear to be nearly commensurate ($\sim 2:3$), but this is likely a coincidence since these periods are changing rapidly in opposite directions. Such commensurability has been seen before in the case of 1P/Halley (8, 16), where it is apparently a stable resonant phenomenon. It is a feature that has been seen in numerical simulations of the evolution of cometary spin (17).

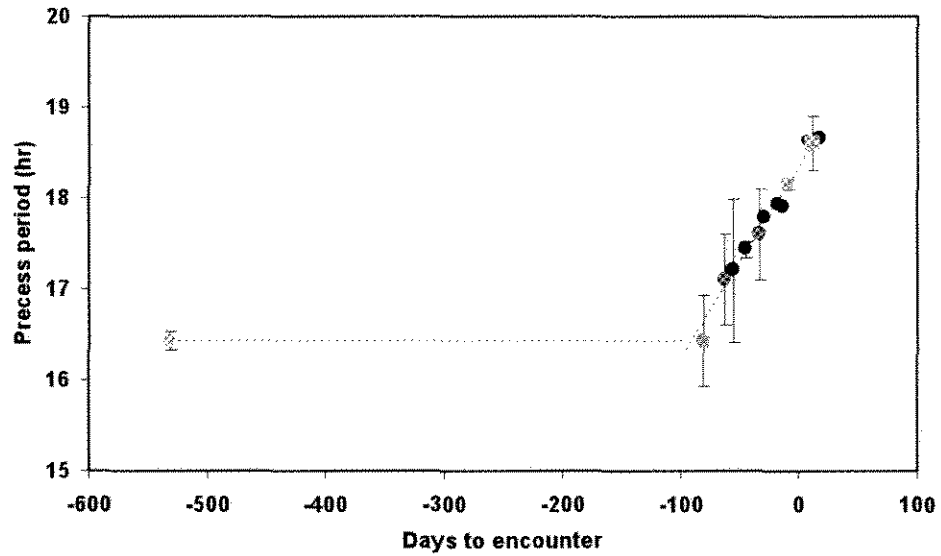


Figure S3. Change in the precessional period of the long axis around the total angular momentum vector as seen from Earth and from the *Deep Impact* spacecraft. Color code for Earth-based observations: grey (11); aqua (12); red (13); gold (14); green (15). The seven EPOXI/DIXI points are in black.

¹ HRI Images used were hv5000005, hv5000022, hv5000065, hv5000095, hv5000118, hv5000139, hv5000152, hv5000152, hv5002000, hv5002015, hv5002028, and hv5002044.

Equipotential Surface

The equipotential model for the surface gravity was used to fit the shape of only the waist. We have not attempted to model the shape of the entire nucleus as an equipotential. The model for the potential includes the effect of the precession of the long axis around the Angular Momentum Vector but does not include the effect of the roll around the long axis. Because the period of roll is long and the lever-arm at the surface is short, the contribution of roll to the potential is unimportant. Figure S4 shows the normalized variance¹ between the observed shape and the calculated potential, in the waist only, as a function of density. The minimum variance is at $\rho = 220 \text{ kg m}^{-3}$, which corresponds to a total mass = $1.84 \times 10^{11} \text{ kg}$. At that minimum, the normalized variance indicates 11% variations of the actual potential around the equipotential. As shown in the figure, the fit deteriorates rapidly for bulk densities less than the best fit value and the waist ceases to be a gravitational low for bulk density $< 180 \text{ kg m}^{-3}$, which would invalidate the assumptions. This sets a lower limit on the density if our assumption of an equipotential is correct. The two lobes would be gravitationally bound to each other, with no strength required, even for densities down to 100 kg m^{-3} . The fit degrades much more slowly for higher values of density. Given the deviations from an equipotential, densities $> 220 \text{ kg m}^{-3}$ are plausible but even 4x higher densities require moderate to high porosity of the bulk material for reasonable assumptions about the rock/ice ratio of the nucleus. The density is clearly in the range found for other, well studied comets such as Tempel 1 at 400 or 450 kg m^{-3} (21, 22), 81P/Wild 2 at 600 kg m^{-3} (23), and 19P/Borrelly at 240 - 490 kg m^{-3} (24, 25). All these determinations are model dependent and have large uncertainties but they are all consistent in being much less than the bulk density of pure ice.

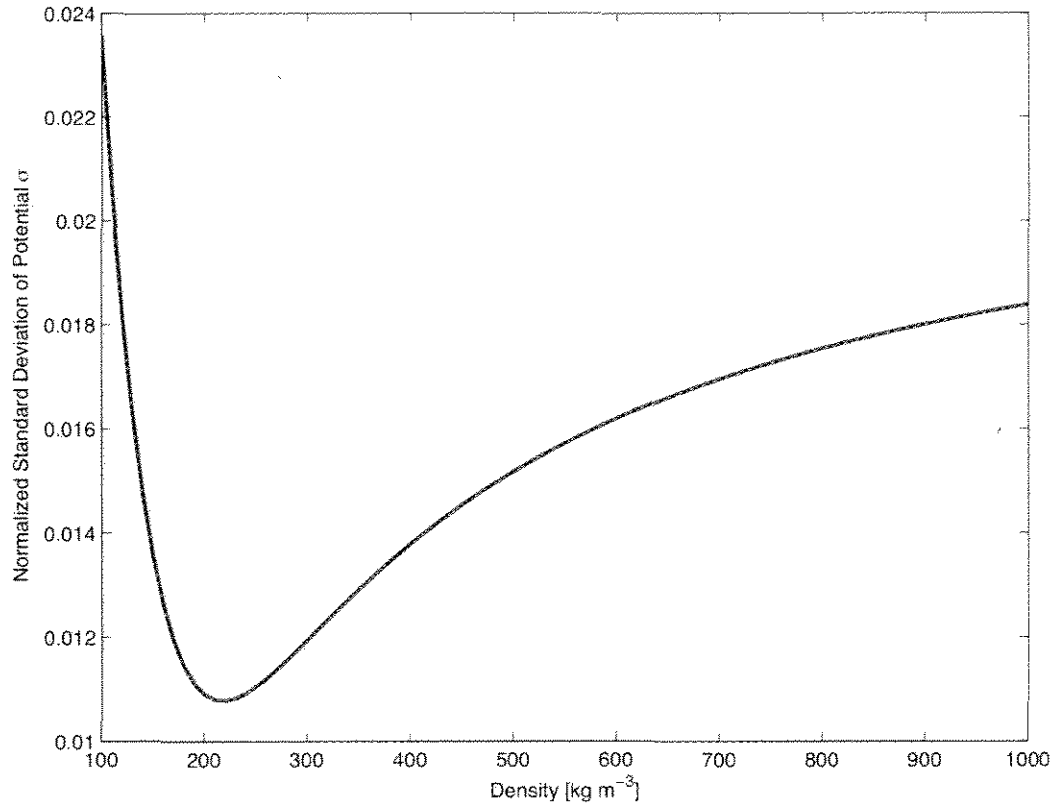


Figure S4. Variance of the potential fitted to the waist of Hartley 2 as a function of assumed density.

¹ The normalized variance is defined as $\sigma_{norm}^2 = \frac{\sum A_i \left(\frac{U_i}{U_A} - 1 \right)^2}{\sum A_i}$ where A_i is the area of the i -th body surface element, U_i is the net potential of the i -th surface element, and U_A is the mean potential. It is thus a measure of the percentage deviations from the equipotential.

CN Anomaly

Routine imaging of the comet began on 5 Sep = E-60d, using primarily a clear filter sensitive to reflected light from grains in the coma and a narrow-band filter isolating an emission band of gaseous CN at 387 nm. The narrow band images were used to derive absolute gas and dust production rates of Hartley 2. To remove the continuum contribution in the CN filter, we assumed an unreddened solar continuum and convolved this with the filter transmission and quantum efficiency of the detector (4). The resulting CN fluxes were used to derive column densities using fluorescent efficiencies scaled to the comet's heliocentric distance and velocity (30). To derive gas production rates, we compared the measured column densities to an image created from a Haser model (31-32) with parent scale length 2×10^4 km & daughter scale length 2×10^5 km, values consistent with the expected lifetimes of HCN and CN against photodissociation. While the spatial distribution of CN released during the comet's regular activity can be described well with this Haser model, the spatial distribution of CN during the anomaly has a significantly shallower slope, suggesting an additional, extended source. A comparison of production of CN (Fig. S5) with the production of water (34) indicates that there was no corresponding increase in water release. A large amount of CN with little or no corresponding dust or water is quite surprising. The spatial profile of CN during the anomaly suggests that the CN was in grains too small or too dark to scatter much sunlight such as HCN polymers (35) or the CHON grains found at 1P/Halley (36). They would need to be lifted by something abundant and volatile. We do not yet have an appropriate physical model for the anomaly since the mechanism for producing the CN in the anomaly is apparently different from the one that operates normally.

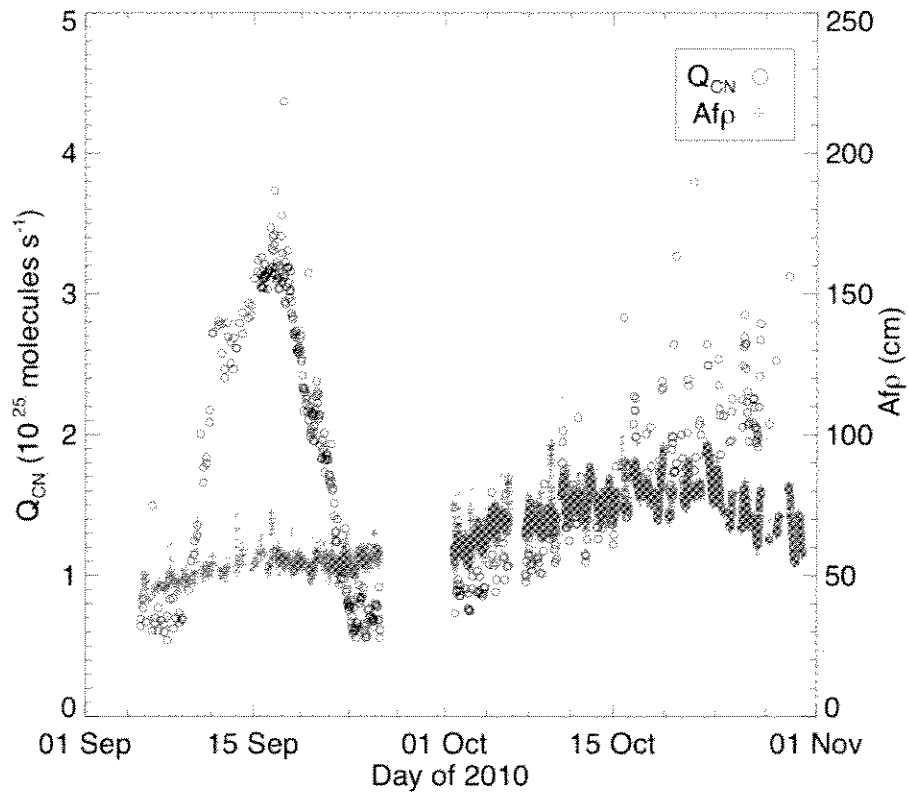


Figure S5. Temporal variation of CN and grain production. CN production in molecules/s compared with the production of grains measured by the parameter A_{fp} (33).

Discrete Chunks

The detailed size distributions and the spatial distributions of the large chunks are shown in figure S6 for a particular MRI image, mv5006001, taken ~1.5 minutes after closest approach. Fluxes were measured in several images in three ways: 1) by aperture photometry of each chunk in calibrated HRI images, 2) by aperture photometry of each chunk in deconvolved, calibrated HRI images, and 3) by fitting a point-spread function to individual chunks in calibrated MRI images. All three approaches lead to consistent results. Completeness was assessed by randomly inserting artificial sources of varying brightness and then finding them in the images using our automated routines. In the size distributions in Figure S6 (upper two panels), points are plotted both as directly measured and after being corrected for incompleteness in recognizing chunks with our software. The same counting data are fitted separately to number as a function of measured flux (proportional to the cross-section of the chunk) and to number as a function of diameter (assuming Europa-like, icy scattering functions; 42-43). We also tried dirty scattering functions based on the nucleus of comet Tempel 1 (44) but consider that less likely as discussed in the main text. Note that the chunks are distributed all around the nucleus without any prominent signs of discrete sources on the nucleus, suggesting that the motions of the grains have become isotropic in the nuclear frame due to the frequently varying gravitational field with every precession period.

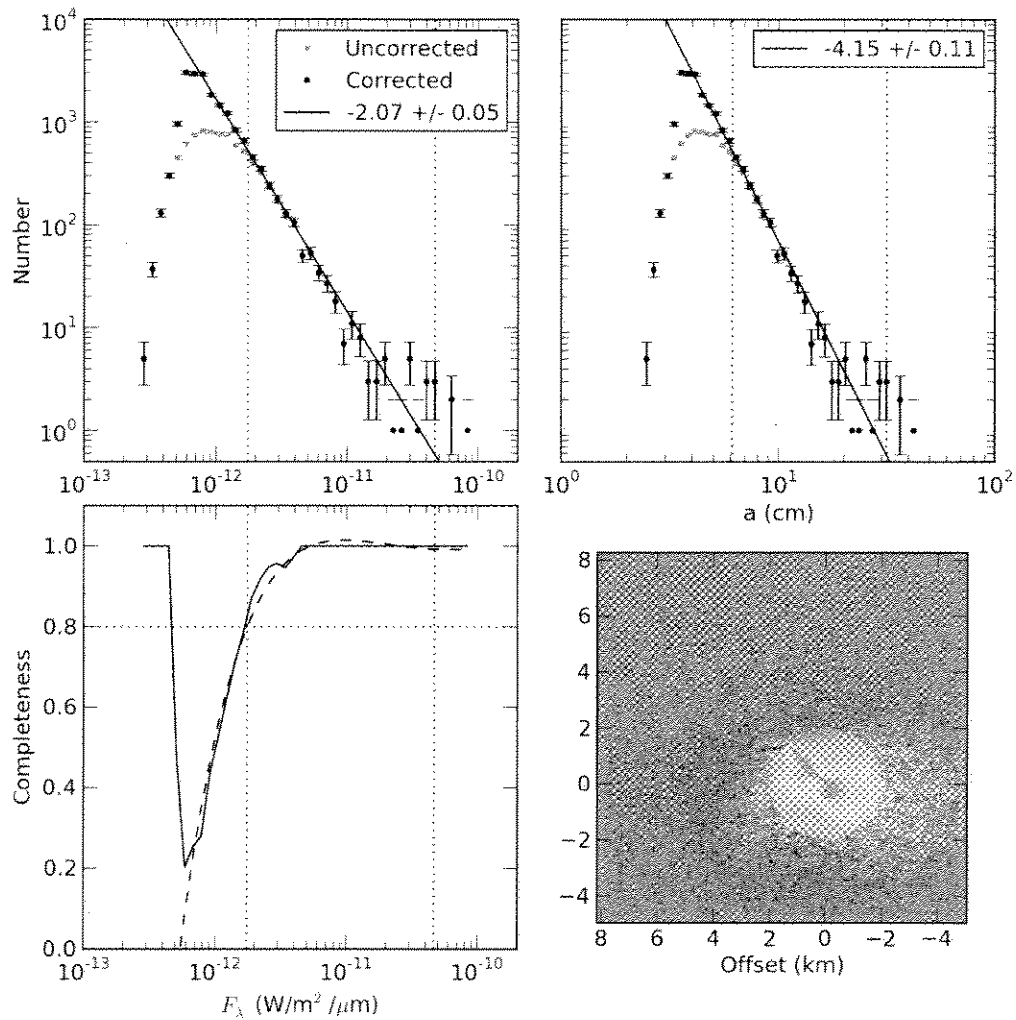


Figure S6. Distribution of chunks seen in MRI image mv5006001. The image was taken 1.5 min after closest approach. Upper left shows the distribution as a function of measured flux from each chunk [$\text{W m}^{-2} \mu\text{m}^{-1}$] while the upper right shows the distribution as a function of diameter [cm] assuming icy chunks. The lower left is an empirical test of the completeness of our counting as a function of the observed flux and is used to correct the actual data in the upper plots. The lower right shows a map of the spatial distribution of the particles in this image with sun at the right.

With an expansion velocity upper-limit of 30 cm s^{-1} , we compute a mass-loss rate in the large chunks alone of 0.5 to $2 \times 10^3 \text{ kg s}^{-1}$, but the uncertainties due to possible sublimation of icy grains and the unknown density of aggregates could alter this number substantially.

Spectral Maps

Spectral processing for each long-slit spectrum includes: a) removal of instrumental thermal background that depends strongly on known quantities such as temperatures inside the spectrometer but also when the most recent previous spectrum was taken and sometimes on the signal in the last previous spectrum; b) correction for non-linearity in the gain of the spectrometer; c) conversion to radiance. Extraction of spectra includes allowance for curvature of the slit as imaged onto the detector (commonly known as spectral “smile”), summing or averaging over spatial pixels both along the slit and from one spectrum to another during a scan. For most purposes, more useful spectra are then obtained by subtracting the continuum, which consists of reflected sunlight at the shorter wavelengths and thermal emission at the longer wavelengths. For the spectra presented in this paper, the continuum has been removed by linearly interpolating between segments of the spectrum thought to be representative of the continuum (reflected sunlight). When only absorption features are of interest, the spectrum is divided by the solar spectrum before subtracting the continuum but this step is omitted when the fluxes of emission features are also of interest. Eventually a proper thermal and scattering model will be used to remove the continuum but this is a major task. From past experience we have limited our conclusions here to ones that will not be affected by improvements to the processing.

Figure 5 was from a spectral scan centered at E+7min consisting of 56 spectra taken over ~2.5 minutes with an exposure time of 1.4 sec per frame during a continuous scan at 1 slit-width per frame. The scan will be available in the PDS archive as image id hi5006000. The maps shown are integrated over the relevant spectral range. A mask was used to suppress the nucleus. The maps have a scale of 52 m/pixel; the maps of the gases are smoothed with a 3x3-pixel box but the map of the ice is not smoothed. All maps are linear in intensity but with varying amounts of stretch. The stretch in the images is best understood by looking at the actual spectra in Figure 6. Those spectra are averages of the surface brightness (radiance) over the boxes and were reduced from the calibrated radiance spectra by fitting straight lines to portions of the spectrum thought to be true continuum. Radiances integrated over the emission bands in the two boxes are: Water-rich waist: $B(\text{H}_2\text{O}) = 1.7 \times 10^{-3}$, $B(\text{CO}_2) = 4.1 \times 10^{-4}$, and Ice-rich lobe: $B(\text{H}_2\text{O}) = 1.1 \times 10^{-3}$, $B(\text{CO}_2) = 8.1 \times 10^{-4}$, all in [$\text{W m}^{-2} \text{sr}^{-1}$]. At this stage of processing, the spectral profile of the organic emission is not yet reliable due to difficulty in separating the ice absorption, the smooth reflected continuum, and the thermal emission, all of which matter at the wavelength of the organics. Because these factors vary from pixel to pixel, the uncertainties in the map of organics are much larger than the uncertainties in the maps of the strong emission features of H_2O and CO_2 . Based on abundances reported from remote sensing for this and other comets, we presume that the emission is dominated by gaseous methanol (CH_3OH), but further discussion of the organic emission is premature.

In order to study the icy grains further, we have calculated models for the reflection spectrum using the optical constants of ice (45) and compared them with the relative reflectance spectrum in Figure S7. The observed spectrum is the same as the one for the ice-rich region in Figure 6, but processed to relative reflectance. In this case, the thermal

emission was subtracted from the observed spectrum as an empirically fit Planck function and the result was divided by the solar spectrum so that any residual “color” due to the scattering properties would remain. It was then normalized at 1.8 μm . The model spectra (46) are for solid spheres of pure, hexagonal ice in an areal mixture with particles assumed to have a reddish slope, characteristic of refractory grains in comets, *i.e.*, the sum of a reddish continuum and a theoretical ice spectrum. The best fit is sensitive to the sizes of the particles but a range of mixing ratios and slopes for the reddish material provides nearly equivalent fits. Archival ID for the data is hi5006000.

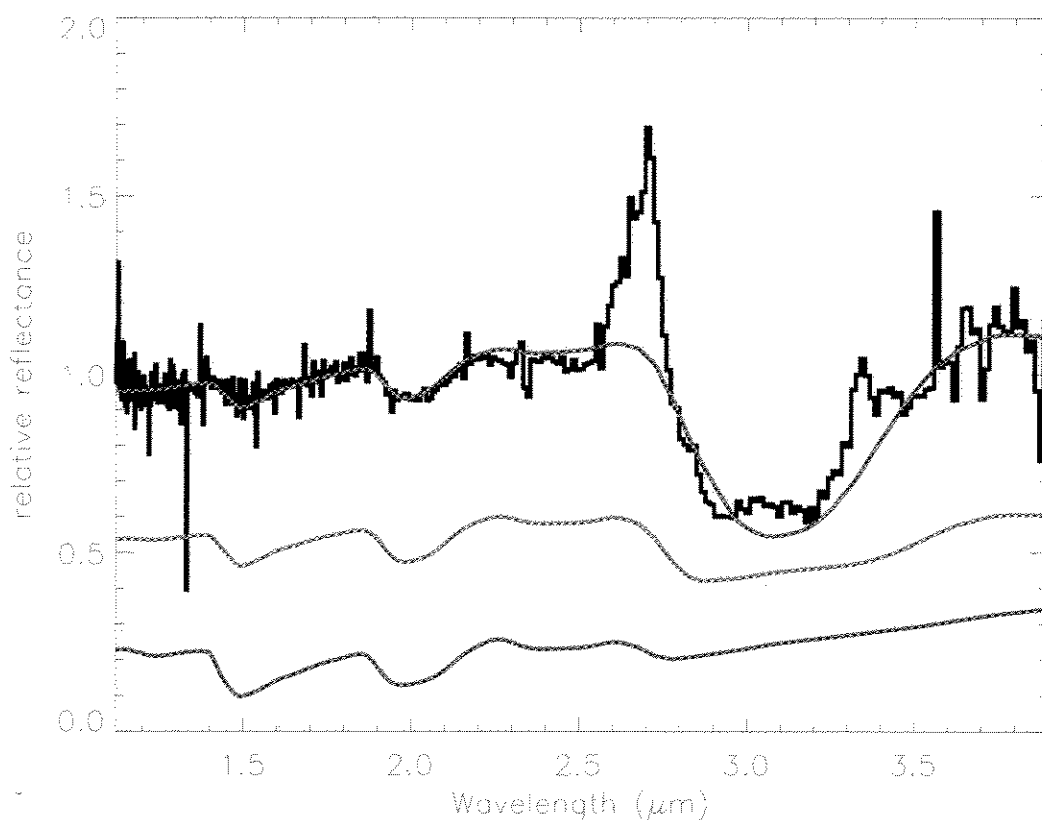


Figure S7 Relative reflectance spectrum of the coma. The smooth curves are theoretical spectra of icy grains of 1 (red), 10 (green), and 100 (purple) μm diameter, normalized to unity at 1.8 μm . The latter two curves have been displaced vertically for clarity. The variation in relative strength of the absorption features at 1.5, 2.0, and 3.2 μm shows that the dominant size of the ice must be less than a few μm .

The fits to the relative reflectance spectrum are primarily sensitive to the size of the icy particles and it is clear that the dominant source of scattered light from the ice must be particles with diameters less than 10 μm . This is consistent with the earlier conclusion that the dominant source of light must be the smallest particles, no matter what the large chunks are. We note that large fluffy aggregates can mimic individual grains of the same size as the constituent pieces of the aggregate and can thus appear small in this type of analysis, even though the actual, porous particles may be much larger. This result is very

similar to the result obtained at Tempel 1 after the impact (no ice was observed prior to the impact). Those grains, which had undergone an excavating shock, were predominantly micron-sized (47). The similarity between excavated material from Tempel 1 and ambient outgassing from Hartley 2 suggests that the constituent solid grains of ice are of order a micron in most comets and that the icy grains seen at Hartley 2 are also from the subsurface.

The spectral map made at E-55 hr was taken from spectral scan hi4000039, integrated over areas of 120×120 km and 600×600 km, centered on the nuclear position (defined by the peak thermal emission) to produce the spectra in Figure S8. The continuum was determined manually and interpolated with straight lines. The interpolation uncertainties could allow some absorption by ice in the 3- μ m band, which would imply a higher total production of water vapor than deduced from these spectra. The band ratio of CO₂/H₂O differs between the two spectra indicating that the optical depth of the bands is still affecting the result in the 120-km box. Average column densities based on an optically thin assumption are: 120-km: N(H₂O) = 6.2×10¹⁵ cm⁻², N(CO₂) = 8.4×10¹⁴ cm⁻²; 600-km: N(H₂O) = 1.7×10¹⁵ cm⁻², N(CO₂) = 3.2×10¹⁴ cm⁻². For simple, radial outflow, the average column density should be inversely proportional to the size of box, but this can be altered either by an extended source of H₂O from the icy grains or by significant optical depth of either species in the 120-km box. For assessing the total release of volatiles, the 600-km box is the better choice.

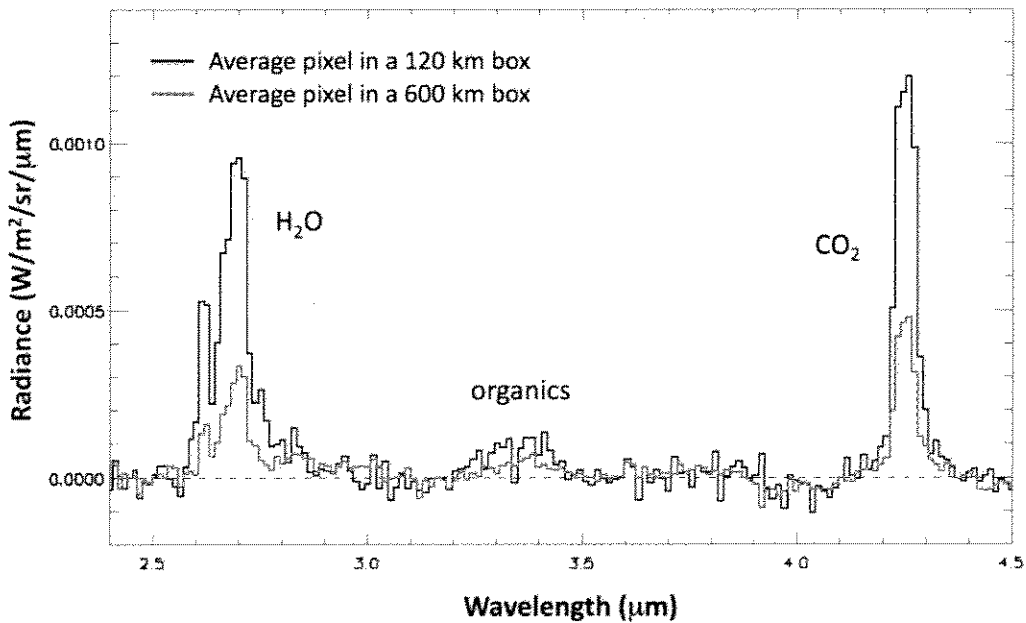


Figure S8. Continuum-removed spectra of Hartley 2 taken 55 hours before closest approach.

The spectra used in Figure 10 were from a large number of short, spatial scans taken at a rapid cadence on departure, hi4300007 through hi4500017. To ensure coverage of the comet by short scans, the rate was set to two slit widths per frame rather than the more usual one slit width per frame. Thus a square box of 5×5 pixels was used to extract

the flux but this actually corresponds to a 10×5 pixel field of view. The range was changing during the period of the scans so the size of the box is not constant in km but is roughly 350×175 km, large enough that the effects of optical depth are minimized.